(article starts on next page)

Astronomy & Astrophysics

Upper limits to interstellar NH$^+$ and para-NH$_2^-$ abundances

Herschel*-HIFI observations towards Sgr B2 (M) and G10.6−0.4 (W31C)**

C. M. Persson[1], M. Hajigholi[1], G. E. Hassel[2], A. O. H. Olofsson[1], J. H. Black[1], E. Herbst[3], H. S. P. Müller[4],
J. Cernicharo[5], E. S. Wirström[1], M. Olberg[1], Å. Hjalmarson[1], D. C. Lis[6], H. M. Cuppen[7],
M. Gerin[8], and K. M. Menten[9]

[1] Chalmers University of Technology, Department of Earth and Space Sciences, Onsala Space Observatory, 439 92 Onsala, Sweden
e-mail: carina.persson@chalmers.se
[2] Department of Physics & Astronomy, Siena College, Loudonville, NY 12211, USA
[3] Department of Chemistry, University of Virginia, McCormick Road, Charlottesville, VA 22904, USA
[4] I. Physikalisches Institut, Universität zu Köln, Zülpicher Str. 77, 50937 Köln, Germany
[5] Centro de Astrobiologìa, CSIC-INTA, 28850 Madrid, Spain
[6] California Institute of Technology, Cahill Center for Astronomy and Astrophysics 301-17, Pasadena, CA 91125, USA
[7] Radboud University Nijmegen, IMM – Faculty of Science, PO Box 9010, 6500 GL Nijmegen, The Netherlands
[8] LERMA-LRA, UMR 8112 du CNRS, Observatoire de Paris, École Normale Supérieure, UPMC & UCP, 24 rue Lhomond,
75231 Paris Cedex 05, France
[9] Max-Planck-Institut für Radioastronomie, Auf dem Hügel 69, 53121 Bonn, Germany

ABSTRACT

The understanding of interstellar nitrogen chemistry has improved significantly with recent results from the *Herschel* Space Observatory. To set even better constraints, we report here on deep searches for the NH$^+$ ground state rotational transition $J = 1.5-0.5$ of the $^2\Pi_{1/2}$ lower spin ladder, with fine-structure transitions at 1013 and 1019 GHz, and the para-NH$_2^-$ $1_{1,1}-0_{0,0}$ rotational transition at 934 GHz towards Sgr B2 (M) and G10.6−0.4 (W31C) using the *Herschel* Heterodyne Instrument for the Far-Infrared (HIFI). No clear detections of NH$^+$ are made and the derived upper limits relative to the total number of hydrogen nuclei are $\lesssim 2 \times 10^{-12}$ and $\lesssim 7 \times 10^{-13}$ in the Sgr B2 (M) molecular envelope and in the G10.6−0.4 molecular cloud, respectively. The searches are, however, complicated by the fact that the 1 013 GHz transition lies only -2.5 km s^{-1} from a CH$_2$NH line, which is seen in absorption in Sgr B2 (M), and that the hyperfine structure components in the 1019 GHz transition are spread over 134 km s^{-1}. Searches for the so far undetected NH$_2^-$ anion turned out to be unfruitful towards G10.6−0.4, while the para-NH$_2^-$ $1_{1,1}-0_{0,0}$ transition was tentatively detected towards Sgr B2 (M) at a velocity of 19 km s^{-1}. Assuming that the absorption occurs at the nominal source velocity of $+64$ km s^{-1}, the rest frequency would be 933.996 GHz, offset by 141 MHz from our estimated value. Using this feature as an upper limit, we found N(p-NH$_2^-$) $\lesssim 4 \times 10^{11}$ cm^{-2}, which implies an abundance of $\lesssim 8 \times 10^{-13}$ in the Sgr B2 (M) molecular envelope. The upper limits for both species in the diffuse line-of-sight gas are less than 0.1 to 2% of the values found for NH, NH$_2$, and NH$_3$ towards both sources, and the abundance limits are $\lesssim 2-4 \times 10^{-11}$. An updated pseudo time-dependent chemical model with constant physical conditions, including both gas-phase and surface chemistry, predicts an NH$^+$ abundance a few times lower than our present upper limits in diffuse gas and under typical Sgr B2 (M) envelope conditions. The NH$_2^-$ abundance is predicted to be several orders of magnitudes lower than our observed limits, hence not supporting our tentative detection. Thus, while NH$_2^-$ may be very difficult to detect in interstellar space, it could, on the other hand, be possible to detect NH$^+$ in regions where the ionisation rates of H$_2$ and N are greatly enhanced.

Key words. ISM: abundances – ISM: molecules – line: formation – submillimeter: ISM – astrochemistry – molecular processes

1. Introduction

An important species in the nitrogen chemistry, NH$^+$, has for a long time been awaiting its first discovery. Besides its key chemical role in the reaction chain leading to more complex nitrogen-bearing species, NH$^+$ has also been identified as a potential candidate for probing variations in the fine-structure constant, α, and electron-to-proton mass ratio, μ (Beloy et al. 2011). Another undetected but interesting species in the nitrogen chemistry is the anion NH$_2^-$.

Searches for NH$^+$ and NH$_2^-$ are, however, difficult not only because of their expected very low abundances, but also since their strongest transitions lie at frequencies that are generally inaccessible to ground-based telescopes. With the launch of *Herschel* (Pilbratt et al. 2010; Roelfsema et al. 2012) and its sensitive Heterodyne Instrument for the Far-Infrared (HIFI), which was designed to perform high-resolution observations at frequencies 480−1250 and 1410−1910 GHz, searches for the fundamental rotational transitions of NH$^+$ and NH$_2^-$ became possible.

Previous searches for NH$^+$ using *Herschel*-HIFI in the diffuse line-of-sight gas towards the high-mass star-forming regions G10.6−0.4 and W49N, resulted in average upper limits of the NH$^+$ abundance relative to molecular hydrogen $\lesssim 4 \times 10^{-10}$, and N(NH$^+$)/N(NH) $\lesssim 4-7\%$ (Persson et al. 2012).

---

* *Herschel* is an ESA space observatory with science instruments provided by European-led Principal Investigator consortia and with important participation from NASA.

** Appendices are available in electronic form at
http://www.aanda.org

Table 1. Observed NH$^+$ and para-NH$_2^-$ transitions.

Species	Frequency[a]	T_C[b]		$1\sigma/T_C$[c]	
		G10.6	SgrB2	G10.6	SgrB2
	(GHz)	(K)	(K)	(K)	(K)
NH$^+$	1012.540[d]	3.3	7.3	0.0019	0.0015
	1019.211[e]	3.3	7.4	0.0022	0.0040
p-NH$_2^-$	933.855[f]	2.6	7.5	0.0035	0.0013

Notes. NH$^+$ was observed in band 4a with the 1013 GHz line in the lower sideband, and the 1019 GHz line in the upper sideband. [a] Frequencies without the nuclear hyperfine structure (hfs; Hübers et al. 2009) that are used to convert frequencies to Doppler velocities relative to the local standard at rest V_{LSR}. Hfs components of NH$^+$ can be found in Tables D.1–D.2. The p-NH$_2^-$ frequency is estimated using spectroscopic data from Tack et al. (1986). [b] The single sideband continuum intensity. [c] The rms noise (for a channel width of 1 km s^{-1}) divided by T_C. [d] $J = 1.5^- - 0.5^+$ (− and + denotes the parity). [e] $J = 1.5^+ - 0.5^-$. [f] $J_{K_a,K_c} = 1_{1,1} - 0_{0,0}$.

In this paper we present the results of new, deeper searches for NH$^+$, and for the first time also for NH$_2^-$, towards G10.6−0.4 and Sgr B2 (M). Both sources are very well-known star-forming regions and extremely luminous sub-millimetre and infrared continuum sources. The ultra-compact H ɪɪ region G10.6−0.4 in the star-forming complex W31 is located in the Galactic 30 km s^{-1} arm at a distance of 4.95 kpc (Sanna et al. 2014), and the Sgr B2 (M) region is one of the chemically rich sources close to the Galactic centre at a distance of 8.5 kpc (e.g. Nummelin et al. 2000; Bergin et al. 2010). We also model the abundances of NH$^+$ and NH$_2^-$ under four different interstellar conditions with a pseudo time-dependent chemical model, and explore how the surface chemistry, cosmic ionisation rate, and assumed initial metal abundances influence the derived abundances.

2. Spectroscopy, observations, and data reduction

The observed transitions are listed in Table 1. Measurements of the two fine-structure transitions in the lowest $N = 1-1$, $J = 1.5-0.5$ rotational transition of NH$^+$ in its $^2\Pi_{1/2}$ lower spin ladder were performed by Verhoeve et al. (1986) and included resolved hyperfine structure (hfs). An energy-level diagram can be found in Hübers et al. (2009, their Fig. 1). The Einstein A values (Tables D.1–D.2) were derived by one of us (HSPM) from these data, using the experimental ground-state electric dipole moment of 1.988 (28) D (Mount et al. 2012), and taking additional parameters from Hübers et al. (2009) into account. The frequency of the $^1A_1$, $J_{K_a,K_c} = 1_{1,1}-0_{0,0}$ NH$_2^-$ transition was taken from the Madrid molecular spectroscopy excitation (MADEX) database (Cernicharo 2011, Table D.3). It was calculated from the spectroscopic parameters reported by Tack et al. (1986). The uncertainties of the infrared transition frequencies are of the order of 100 MHz. While statistics may improve the prediction of transition frequencies, correlation among the spectroscopic parameters or vibration-rotation interaction may lead to significantly increased uncertainties. Botschwina et al. (1993) calculated a ground-state dipole moment of 1.311 D with an estimated uncertainty of 0.01 D.

Emission or absorption features of other species were assigned by consulting the Cologne Database for Molecular Spectroscopy (CDMS) (Müller et al. 2001, 2005), Jet Propulsion Laboratory (JPL) (Pickett et al. 1998), or MADEX catalogues.

Specifically, the NH$_2$ (Gendriesch et al. 2001), CH$_2$NH (Dore et al. 2012), and SO$_2$ (Müller & Brünken 2005) entries were taken from the CDMS catalogue while the methanol entry (Xu et al. 2008) was taken from the JPL catalogue.

The observations, which took place in April and September 2012, are summarised in Table 1 and the observational identifications are found in the on-line Table D.4. We used the dual beam switch mode and the wideband spectrometer (WBS) with a bandwidth of 4×1 GHz and an effective spectral resolution of 1.1 MHz ($\Delta v = 0.3$ km s^{-1}). Two orthogonal polarisations were used in all the observations. All lines towards G10.6−0.4 were observed with three different overlapping frequency settings of the local oscillator (LO) to determine the sideband origin of the lines since HIFI uses double sideband (DSB) receivers. Towards Sgr B2 (M) we used the spectral scan mode and eight different overlapping LO settings because of its extreme density of emission lines.

The pointings were centred at $\alpha = 17^h47^m20\overset{s}{.}6$, $\delta = -28°23'03.2''$ (J2000) for Sgr B2 (M), and $\alpha = 18^h10^m28\overset{s}{.}7$, $\delta = -19°55'50.0''$ (J2000) for G10.6−0.4. The source systemic velocities are 58–69 and −3 km s^{-1} for Sgr B2 (M) and G10.6−0.4, respectively. Absorptions in the source molecular clouds are centred at +64 and −0.5 km s^{-1}, and the foreground gas along the respective sight-line is detected in absorption from −140 to 27, and 10 to 55 km s^{-1}.

The data were reprocessed using the hifiPipeline task in HIPE version 9.0, up to level 2 providing fully calibrated DSB spectra for G10.6−0.4 on the T_A^* antenna temperature intensity scale where the lines are calibrated to single sideband (SSB) and the continuum to DSB. For the Sgr B2 (M) observations, we used in addition the doDeconvolution task up to level 2.5 to provide fully calibrated SSB spectra. The FitHifiFringe task was then used to fit and remove residual ripples in the spectra, except for the NH$^+$ 1 019 GHz data towards Sgr B2 (M) since this spectrum had too many spectral features. The G10.6−0.4 data quality is excellent with very low intensity ripples, with good agreement between the three LO-tunings, and without any visible contamination from the image sidebands.

The FITS files were exported to the spectral line software package xs[1], which was used in the subsequent data reduction. All tunings and both polarisations were included in the averaged noise-weighted spectra for all transitions, which were convolved to a channel width of 1 km s^{-1}. Baselines of order five were removed from the G10.6−0.4 spectra, and of order three and seven from the Sgr B2 (M) NH$_2^-$ and NH$^+$ 1013 GHz spectra (average T_C added afterwards). No baseline was removed from the Sgr B2 (M) NH$^+$ 1019 GHz spectrum.

3. Results

Figures 1–2 show the averaged WBS spectra of all observed transitions as a function of the local standard of rest velocity, V_{LSR}. The continuum and rms are given in Table 1. We performed an unbiased search for emission and absorption lines from NH$^+$ and para-NH$_2^-$ in the source molecular clouds, and absorption from diffuse or translucent gas along the lines-of-sight. Despite the low noise levels, no detections are found in the G10.6−0.4 data (Fig. 1). Column densities are therefore 3σ upper limits, estimated with a typical line width (4 km s^{-1}) and the total line-of-sight velocity range. The emission line visible in the

---

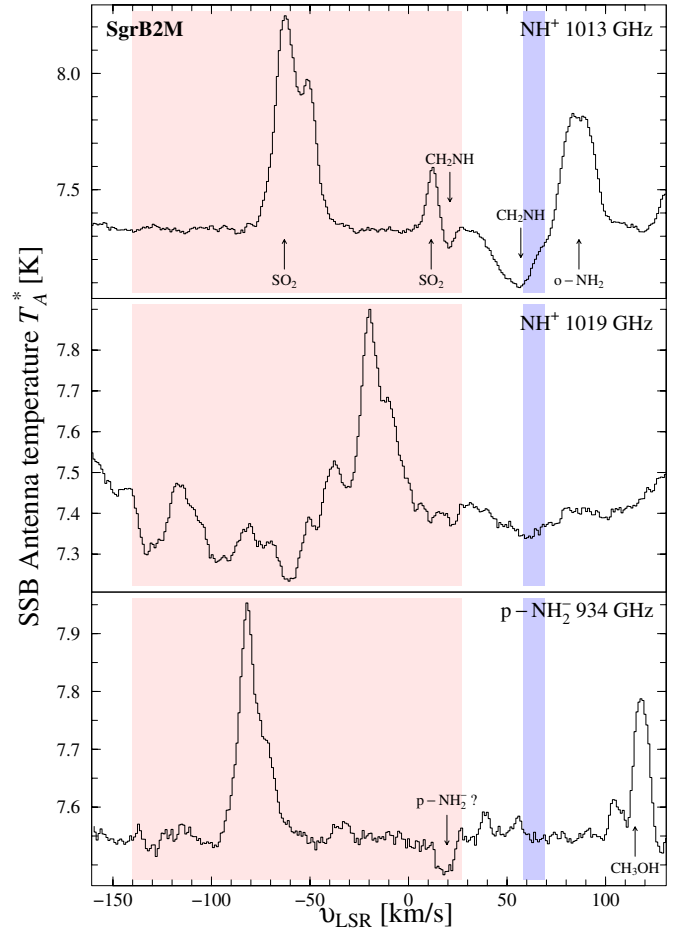[1] http://www.chalmers.se/rss/oso-en/observations/data-reduction-software
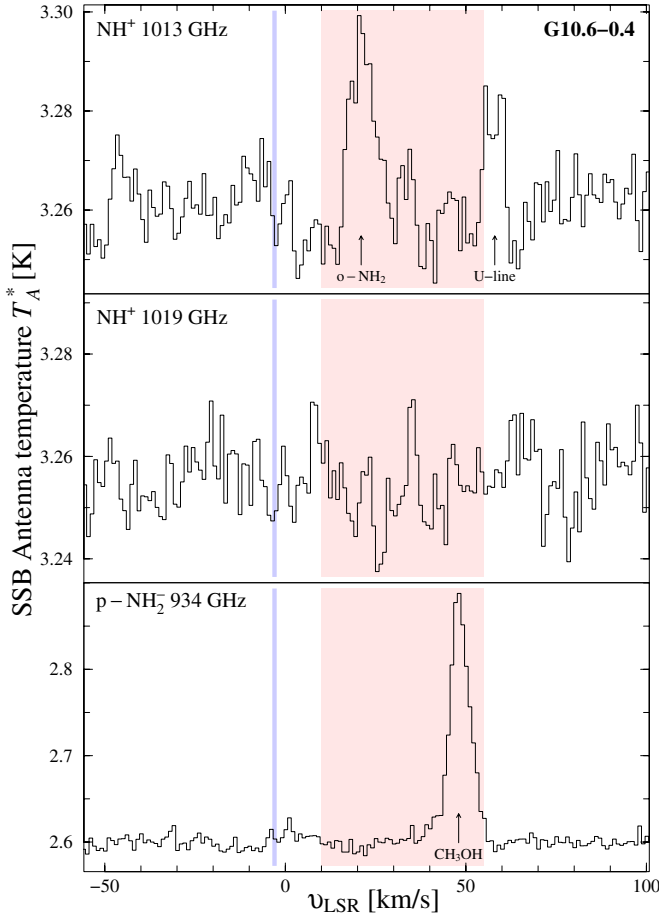
Fig. 1. G10.6−0.4: searches for NH$^+$ and p-NH$_2^-$ show no detections at the source velocity −3 km s^{-1} (marked in blue) or the line-of-sight absorption at 10–55 km s^{-1} (marked in red). The ortho-NH$_2$ and CH$_3$OH emission lines originate in the G10.6−0.4 molecular cloud.

Fig. 2. Sgr B2 (M): searches for NH$^+$ and p-NH$_2^-$ show no clear detections at the source molecular cloud velocities 58–69 km s^{-1} (marked in blue) or the line-of-sight absorption between −140 and 27 km s^{-1} (marked in red). Possible weak NH$^+$ absorption from the molecular cloud is blended with the stronger CH$_2$NH absorption. Para-NH$_2^-$ is tentatively detected from the source molecular cloud, however, at V_{LSR} = 19 km s^{-1}. All emission lines originate in the Sgr B2 (M) molecular cloud.

NH$^+$ 1013 GHz band (upper panel) at +21 km s^{-1} is identified as ortho-NH$_2$ $4_{2,2}-4_{1,3}$.

Towards Sgr B2 (M), we find two absorption features at $V_{LSR} \approx 60$ km s^{-1} in both NH$^+$ spectra (upper and middle panels in Fig. 2). It is to be noted that the 1013 and 1019 GHz lines are expected to show very different line profiles since they both have 14 hfs components and are spread over velocity ranges of 26 and 134 km s^{-1}, respectively. To check whether the observed line profiles fit the respective NH$^+$ hfs, we model the absorption of both lines using Gaussian optical depth profiles generated for each hfs component. These profiles are made to fit the observations under the condition that the V_{LSR} and line width are the same for both transitions (cf. Method I in Persson et al. 2012). Assuming a sideband gain ratio of unity, we calculate the line opacities as $\tau = -\ln(T_A^*/T_C)$, where T_A^* is the SSB antenna temperature. As seen in Fig. A.1 (on-line material) the fit to the 1013 GHz line shows a very good agreement with the observed line profile, whereas the 1019 GHz fit suggests either that the detection is not real, or that a considerable part of the absorption comes from other species, or that it is (partly) caused by remaining ripples which we were not able to remove.

Despite the agreement of the fits, we ascribe the largest part of the feature in the 1013 GHz spectrum to CH$_2$NH. This species has two transitions with similar line strengths close to NH$^+$ at 1013 GHz: $3_{3,1}-2_{2,0}$ (with E_l = 41 K) only +8.5 MHz (−2.5 km s^{-1}) from the NH$^+$ line, and $3_{3,0}-2_{2,1}$ seen as a narrow

absorption at 21 km s^{-1} in Fig. 2 (upper panel). This line, however, blends with the SO$_2$ $41_{5,37}-40_{4,36}$ (1 012.673 GHz) emission and is therefore easily missed. Our identification is also supported by previous observations of CH$_2$NH in both absorption ($1_{1,1}-0_{0,0}$) and emission towards Sgr B2 (M) (Nummelin et al. 2000). We modelled the SO$_2$ emission, both CH$_2$NH absorptions, and the o-NH$_2$ $4_{2,2}-4_{1,3}$ emission line wing (seen at ~70 km s^{-1} in Fig. 2, upper panel) in order to subtract these lines in the search for any remaining weak NH$^+$ absorption. More details of the modelling are found in on-line Sect. A, and all modelled lines are shown in Fig. A.2. After subtraction of the modelled lines, we find a weak remaining absorption feature at V_{LSR} = 69 km s^{-1} with an integrated opacity of 0.08 km s^{-1}. This feature is considered as an upper limit of NH$^+$ in the SgrB2 (M) molecular envelope. An unidentified remaining absorption feature is also seen at 45.5 km s^{-1} with an integrated opacity of 0.19 km s^{-1}. Both these features are, however, very weak and may well be remaining artefacts from our modelling or ripples in the baseline.

In the 934 GHz band we find an unidentified absorption feature at $V_{LSR} \approx$ +18.5 km s^{-1} towards Sgr B2 (M) with a line width of ≈9 km s^{-1} and an integrated opacity of 0.09 km s^{-1}

Table 2. Resulting NH^+ and NH_2^- column densities, N, column density ratios with related species, and abundances, X, with respect to the total amount of hydrogen towards Sgr B2 (M) and G10.6−0.6.

Source	V_{LSR}	$N(NH^+)$	$\frac{N(NH^+)}{N(NH)}$	$\frac{N(NH^+)}{N(NH_2)}$ [b]	$\frac{N(NH^+)}{N(NH_3)}$ [c]	$N(p\text{-}NH_2^-)$	$\frac{N(p\text{-}NH_2^-)}{N(NH_2)}$ [b]	$\frac{N(p\text{-}NH_2^-)}{N(NH_3)}$ [c]	$X(NH^+)$	$X(p\text{-}NH_2^-)$
	(km s^{-1})	(cm^{-2})	(%)	(%)	(%)	(cm^{-2})	(%)	(%)		
				Line-of-sight[a]						
Sgr B2 (M)	−140-27	≲1.7×10^{12}	≲0.1	≲0.2	≲0.2	≲9.9×10^{11}	≲0.1	≲0.1	≲4×10^{-11d}	≲2×10^{-11d}
G10.6−0.6	10-55	≲1.6×10^{12}	≲0.9	≲1.5	≲1.9	≲2.2×10^{12}	≲1.9	≲2.6	≲3×10^{-11e}	≲4×10^{-11e}
				Source molecular cloud/envelope						
Sgr B2 (M)	57–68	≲9.1×10^{11}	...	...	...	≲4.0×10^{11}	...	...	≲2×10^{-12f}	≲8×10^{-13f}
G10.6−0.6	−3	≲2.8×10^{12}	...	...	...	≲2.0×10^{12}	...	...	≲7×10^{-13g}	≲5×10^{-13g}

Notes. [a] The limits are estimated over the velocity ranges listed in Col. (2). [b] Using the high temperature ortho-to-para (OPR) limit of 3 for NH_2. [c] Using OPR(NH_3) = 0.7 (Persson et al. 2012). [d] $N_H = 2N(H_2) + N(H) = 4.3 \times 10^{22}$ cm^{-2} (Garwood & Dickey 1989; Monje et al. 2011). [e] $N_H = 2N(H_2) + N(H) = 5.6 \times 10^{22}$ cm^{-2} ($N(H)$ from Winkel et al. (in prep.) and $N(H_2)$ from Godard et al. 2012). [f] $N_H \approx 2 \times N(H_2) = 5 \times 10^{23}$ cm^{-2} in the Sgr B2 (M) molecular envelope (Lis & Goldsmith 1989). [g] $N_H = 2 \times N(H_2)/2 = 4 \times 10^{24}$ cm^{-2} in the G10.6−0.4 molecular cloud (Fazio et al. 1978) assuming that NH^+ and NH_2^- are most likely to be seen in absorption thereby probing half of the total column density that is in front of the continuum source.

(lower panel in Fig. 2). This feature is used as an upper limit to the para-NH_2^- $1_{1,1}$−$0_{0,0}$ line. If the absorption is caused by para-NH_2^-, it implies a rest frequency of 933.973–934.009 GHz for this transition, which is 118–154 MHz higher than our estimated frequency assuming that the nominal source velocity is between 56 and 68 km s^{-1}. Results of quantum chemical calculations on NH_2^- were recently reported employing high level coupled cluster calculations with additional correction and large basis sets with extrapolation to infinite basis set size (Huang & Lee 2009). Using their best spectroscopic parameters, a frequency of 932.726 GHz is derived for the $J = 1_{1,1}$−$0_{0,0}$ transition. The level of agreement with the value derived from the experimental spectroscopic parameters corresponds to the one expected under favourable conditions and does not permit exclusion of the Sgr B2 (M) absorption feature as being potentially due to NH_2^-.

We convert the upper limits of NH^+ opacities to column densities with the non-equilibrium homogeneous radiative transfer code RADEX[2] (van der Tak et al. 2007) to correct for possible population of molecules in unobserved excited levels. We use $n(H_2) = 70$ cm^{-3} and a kinetic temperature $T_K = 100$ K for the diffuse line-of-sight conditions, and $n(H_2) = 10^2$−10^4 cm^{-3} and $T_K = 20$−40 K for the denser envelopes of the source molecular clouds. The results are not very sensitive to changes in density because of the high critical density of the nitrogen hydrides ($n_{crit} \sim 10^8$ cm^{-3}). For the line-of-sight, we use the average Galactic background radiation in the solar neighbourhood plus the cosmic microwave background radiation as background radiation field. In addition, for the source molecular clouds we include their respective observed spectral energy distribution.

Since no collisional coefficients are available for NH_2^-, we estimate the column density of molecules in the ground-state using

$$N_l(p - NH_2^-) = 8\pi \frac{v^3}{c^3} \frac{g_l}{g_u A_{ul}} \int \tau dV = 4.7 \times 10^{12} \int \tau dV \; [\text{cm}^{-2}]. \tag{1}$$

The resulting upper limits for the column density and abundance with respect to the total column of hydrogen are found in Table 2. Here we also present limiting abundance ratios, relative to the chemically related species NH, NH_2, and NH_3

---

[2] http://www.sron.rug.nl/~vdtak/radex/index.shtml

along the line-of-sight gas towards both sources. Column densities towards G10.6−0.4 (averaged over $V_{LSR} = 10$−55 km s^{-1}) are taken from Persson et al. (2012). A full spectral scan of Sgr B2 (M) using *Herschel*-HIFI has been performed by the HEXOS Key Programme (Bergin et al. 2010). From these data, spectra of the ground-state rotational transitions of NH, NH_2, and NH_3 were extracted and compared to our data. Resulting ratios are consistent with the findings in Persson et al. (2010), and $N(NH_3)$ is in agreement with Wirström et al. (2010). We reduced these data in a manner similar to that described in Sect. 2 for our Sgr B2 (M) data, and fitted Gaussian optical depth profiles to the absorption lines to estimate the column densities.

4. Chemical modelling

In Persson et al. (2010) we modelled abundances of the nitrogen hydrides with a pseudo time-dependent chemical model with constant physical conditions, taking both the gas-phase and grain surface chemistry into account, using the Ohio State University (OSU) gas-grain code (Hasegawa et al. 1992). The predicted NH^+ abundance was at most $\sim 10^{-13}$−10^{-14} in translucent clouds with $A_V = 2$−3.

In this paper, we have updated the chemical models to include the formation and destruction of NH_2^-. The expanded reaction network also includes high temperature reactions (Harada et al. 2010; Hassel et al. 2011) and presently considers 7176 reactions involving a total of 669 gaseous and surface species.

Figure 3 shows two chemical networks outlining the major reaction pathways involving nitrogen hydrides at $t = 10^6$ years, under translucent and diffuse gas conditions. In both cases, the production of NH^+ purely by gas-phase processes largely depends on a sufficient source of N^+, which can be formed by cosmic ray ionisation of N or by reactions of He$^+$ with N_2 or CN. It should be noted that H_3^+ does not react rapidly with N, hence the latter route is the most important one in denser gas, while the former dominates in diffuse gas. In standard gas-phase ion-molecule chemistry, NH^+ then initiates the production of nitrogen hydrides (NH, NH_2, and NH_3) via subsequent reactions with H_2 and electron recombination. This is, however, not effective in diffuse gas where hydrogen exists mostly in atomic form. Included in the chemical networks of Fig. 3 is also the surface reaction pathway for the formation of nitrogen hydrides,
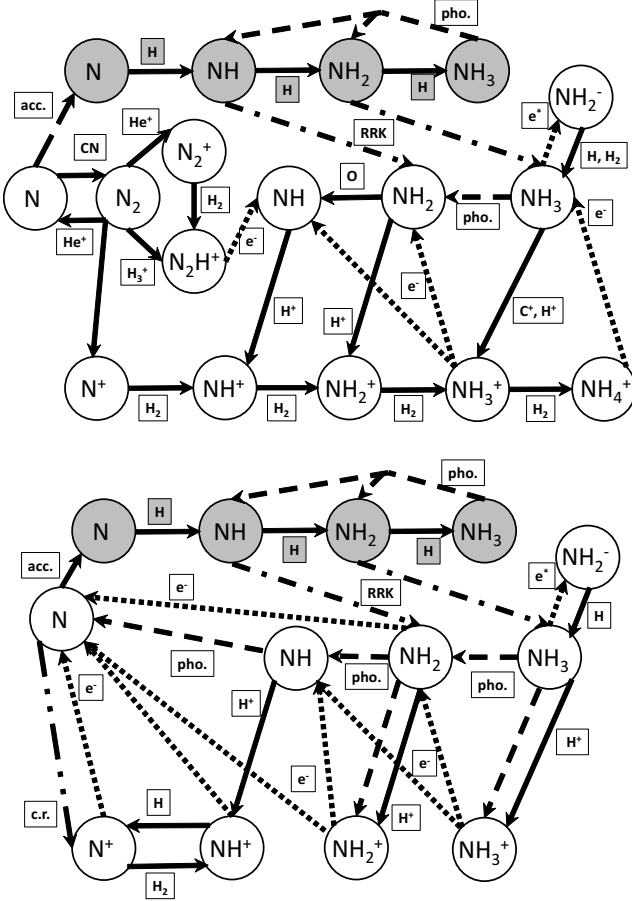
Fig. 3. Major formation paths of nitrogen hydrides at $t = 10^6$ years for translucent gas conditions (*upper panel*) and diffuse gas conditions (*lower panel*). Gas phase species appear in white and grain surface species in grey. Solid lines indicate gas phase reactions, dashed lines photo-dissociation, dotted lines dissociative recombination, electronic radiative recombination and attachment processes, and dot-dashed lines non-thermal desorption from the grain surfaces.

in which H atoms are added to N, and NH_3 is in turn destroyed by photo-dissociation. The species NH_2 and NH_3 can then be liberated into the gas phase through non-thermal desorption via the Rice-Ramsperger-Kassel (RRK) mechanism (Garrod et al. 2006, 2007), where the species desorb as a result of exothermic surface reactions with an efficiency governed by the parameter a_{RRK}, which is typically set to 0.01. We have also considered the addition of photodesorption of NH_3 with an assumed yield of $Y_{PD} = 10^{-3}$ molecules/UV photon in the absence of a measured yield, based on the formulation of Öberg et al. (2007) for desorption of CO by both the direct interstellar radiation field and the field caused by cosmic rays. The direct photodesorption process is of secondary importance to the RRK mechanism for the formation of NH_3(gas) in the translucent gas models and of even lesser importance in the diffuse gas models. In the diffuse model, the major form of nitrogen is predominantly elemental N at 10^6 yrs, while in the the translucent model, elemental N, NH_3(ice), and N_2(gas) are the major forms. In addition to the processes shown here, there are some minor processes, such as $O + CN \rightarrow CO + N$, $C + NO \rightarrow N + CO$, and $NO^+ + e^- \rightarrow N + O$, that return some elemental N to the gas phase from less abundant forms, but these are omitted from Fig. 3.

The abundance of NH^+ thus directly depends on a N^+ source and the cosmic ionisation rate $\zeta(H_2)$. Radiative recombination of N^+ is a slow process; therefore, in the presence of just a small H_2 fraction, N^+ is removed mainly by $N^+ + H_2 \rightarrow NH^+ + H$, which is the source reaction of NH^+. Thus almost every cosmic ray ionisation of N will produce NH^+. Reactions with H_2 and with electrons removes NH^+, but the reactions with H_2 dominate as long as $e^-/H_2 \lesssim 0.001$. Within this limit, independent of density and temperature, the NH^+ fractional abundance is of the order of 10^{-12} at $n(H_2) \approx 100$ cm^{-3} and $X(N) \approx 10^{-4}$.

The NH_2^- anion can form via the dissociative attachment process through electron-impact on NH_3

$$e^* + NH_3 \rightarrow NH_2^- + H, \tag{2}$$

where e^* represents an energetic electron. The energetic threshold for this process is $\varepsilon = 3.857$ eV. The possible destruction processes of NH_2^- include photo-detachment, reactions with H_2, and mutual neutralisation in reactions with the most abundant positive ions. If the reaction with H_2 is the dominant loss process, then the density of NH_2^- at $T = 50-100$ K will be of the order of

$$n(NH_2^-) \sim 7 \times 10^{-8} \frac{n(NH_3)}{n(H_2)} \ [\text{cm}^{-3}], \tag{3}$$

which immediately suggests a very low NH_2^- abundance. A second formation route of NH_2^- is via slow radiative attachment of electrons to NH_2

$$NH_2 + e^- \longrightarrow NH_2^- + h\nu. \tag{4}$$

Finally, if the anion is formed in a local region rich in atomic rather than molecular hydrogen, it can be destroyed by associative attachment with atomic hydrogen,

$$NH_2^- + H \longrightarrow NH_3 + e^-, \tag{5}$$

or competitively via photo-detachment. Details about the different formation and destruction routes of NH_2^- are found in Appendix B.

Figure 4 shows the resulting temporal evolution of the NH^+ and NH_2^- abundances using the updated chemical network and a typical active non-thermal desorption efficiency $a_{RRK} = 0.01$. We have modelled both species under four different physical conditions: typical dense gas, translucent gas, diffuse gas, and a special model for the Sgr B2 (M) molecular envelope. All model parameters are found in Table 3.

The choice of initial elemental abundance values vary for the different models. For the translucent and dense models, we adopt "low metal" initial abundances, whereas we adopt a set of "high metal" initial abundances for the diffuse and Sgr B2 (M) models. The "low metal" values account for the incorporation of elements into refractory grains on the basis of observations of ζ Oph (Graedel et al. 1982; Garrod et al. 2007), and the "high metal" values were developed to estimate the abundances if all of this material initially existed in the gas phase (Wakelam & Herbst 2008; Garrod & Herbst 2006). The different values are listed in Table D.5, and the effects of the adoption on abundance of NH^+ is explored in Fig. C.1, where the choice of high metal abundances can be seen to increase the abundance of NH^+ towards the observational upper limit for the diffuse model. The same trend is found for the Sgr B2 (M) and dense models, however, not for the translucent model.

The dense models are representative of the massive sources themselves, the translucent cloud conditions are traced by, for
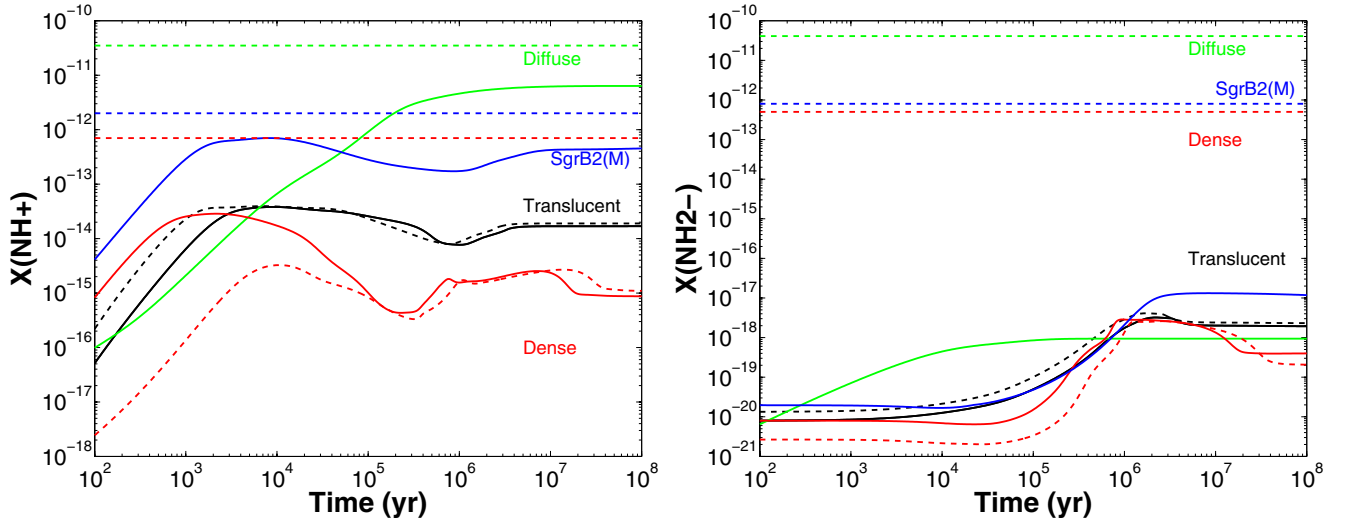
Fig. 4. Temporal evolution of the NH$^+$ (*left*) and NH$_2^-$ (*right*) abundances using gas and surface chemistry and a typical active non-thermal desorption efficiency $a_{RRK} = 0.01$ using four different sets of conditions (see Table 3). Typical diffuse cloud conditions in green, translucent cloud conditions in black, dense cloud conditions in red, and a special model for the Sgr B2 (M) molecular envelope in blue. The solid and dashed lines represent $T_K = 30$ K and 50 K (translucent model) and $T_K = 30$ K and 10 K (dense model), respectively. The observed upper limits from both species (Table 2) in dense gas (from W31C), diffuse gas (similar limits for both sight-lines), and in the Sgr B2 (M) molecular envelope are indicated by dashed horizontal lines following the respective colour code.

Table 3. Chemical models.

Model	A_V	$n_H{}^a$	T_K	T_{dust}	$\zeta(H_2)^b$	Metallicity^c
	(mag)	(cm^{-3})	(K)	(K)	(s^{-1})	
Diffuse^d	0.5	70	100	17	2×10^{-16}	High
Translucent^d	3	5×10^3	30 & 50	10	1.3×10^{-17}	Low
Dense^d	10	2×10^4	10 & 30	10	1.3×10^{-17}	Low
Sgr B2 (M) envelope^e	300	4×10^3	40	10	4×10^{-16}	High

Notes. All models use a ultraviolet flux of 1 G$_0$. $^{(a)}$ The total hydrogen density $n_H = 2n(H_2) + n(H)$. $^{(b)}$ The cosmic ionisation rate of molecular hydrogen (cf. Indriolo et al. 2012). $^{(c)}$ The assumed initial metal abundances are found in Table D.5. $^{(d)}$ Typical conditions in respective cloud type (e.g. Snow & McCall 2006). $^{(e)}$ Lis & Goldsmith (1989), van der Tak et al. (2006) and Ott et al. (2014).

example, the NH, NH$_2$, and NH$_3$ absorptions along the sight-lines (Persson et al. 2012), and the diffuse cloud conditions are representative of the line-of-sight clouds, from where we believe NH$^+$ originates. The Sgr B2 (M) model reflects the very special conditions found in this source. In Fig. C.2 we show the four models again, but this time with the addition of NH, NH$_2$, and NH$_3$ for comparative purposes. We note that the above results for the translucent model are very similar to the models from Persson et al. (2010).

To check how the surface chemistry affects the resulting abundances we also show (i) gas and surface chemistry and inactive non-thermal desorption efficiency $a_{RRK} = 0$; (ii) gas and surface chemistry with two different a_{RRK} desorption efficiencies; and (iii) pure gas phase chemistry for the translucent model in Fig. C.3 (on-line material). This figure, as well as Fig. 3, illustrates that the surface chemistry with reactive desorption is a key factor in the formation of NH$_2$ and NH$_3$, followed in importance by the addition of electrons to NH$_4^+$. We find, however, that our models are not very sensitive to the exact value of the desorption probability, since the model with $a_{RRK} = 0.1$ gives very similar results to the model using $a_{RRK} = 0.01$.

Since a high cosmic ray ionisation rate is crucial for the production of NH$^+$, our results are sensitive to its assumed value.

In the on-line Fig. C.4 we show, therefore, how the NH$^+$ abundance varies in the diffuse model using seven different values of $\zeta(H_2)$. The NH$^+$ abundance increases by more than an order of magnitude and reaches the observational limit when $\zeta(H_2)$ increases from 10^{-17} to 10^{-14} s^{-1}. The other models also show similar trends.

The rotational transitions of NH$^+$ observed by us provide a sensitive way to search for this ion in absorption. There are also other kinds of transitions suitable, however, for interstellar absorption studies as pointed out by de Almeida & Singh (1982). For example, the ground-state Λ-doubling transition at 13.6 GHz is observable from Earth and now has well determined hfs frequencies (Hübers et al. 2009). If we neglect hfs in both the lowest pure-rotational and Λ-doubling transitions and consider a column density of $N(\text{NH}^+) \sim 10^{12}$ cm^{-2}, then the integrated optical depths in the 1013 and 1019 GHz lines are $\int \tau dv \sim 0.15$ km s^{-1} while the corresponding integrated optical depth at 13.6 GHz is ~ 0.005 km s^{-1}. The electronic transitions at blue and ultraviolet wavelengths are slightly more sensitive than the 13.6 GHz transition. Based on the oscillator strengths tabulated by de Almeida & Singh (1982), the corresponding values of $\int \tau dv$ are 0.009, 0.01, and 0.007 km s^{-1} in the A $^2\Sigma^- - $ X $^2\Pi_r$ (0,0), (1,0), and (2,0) bands near 464, 434, and 410 nm wavelength, respectively.

The ultraviolet band C $^2\Sigma^+$ – X $^2\Pi_r$ (0, 0) near 289 nm will yield $\int \tau \mathrm{d}v \sim 0.009$ km s^{-1} under the same conditions. The existing upper limits on visible and UV lines of NH$^+$ (Snow 1976, 1980; Jenkins et al. 1973) were not very sensitive compared to the submm-wave results presented here. As far as we are aware, no limits have been derived from more modern optical data. Possible archival spectra of stars behind diffuse molecular clouds in which equivalent widths of $W_\lambda \lesssim 1$ mÅ could easily be measured in the 434 nm band corresponding to a column density $\lesssim 6 \times 10^{11}$ cm^{-2}, slightly better than the best limit in Table 2.

5. Conclusions

Our derived NH$^+$ upper limits are an order of magnitude lower than previous estimates (Persson et al. 2012). On the other hand, our chemical modelling suggests that the NH$^+$ abundance may still be a few times lower than our present limits in diffuse gas and under typical Sgr B2 (M) molecular envelope conditions, and several orders of magnitude lower in translucent and dense gas. Since a high ionisation rate is crucial for high NH$^+$ abundances, future searches should focus on regions with greatly enhanced ionisation rates (cf. Indriolo et al. 2012). Searches for NH$^+$ are, however, complicated by the fact that one of its lowest rotational transitions at 1 013 GHz lies only -2.5 km s^{-1} from the $3_{3,1}-2_{2,0}$ CH$_2$NH line seen in absorption in Sgr B2 (M).

In contrast to NH$^+$, the NH$_2^-$ anion has very low abundances in all models, not supporting our tentative detection in Sgr B2 (M). This suggests that this species will be very difficult to detect in interstellar space.

References

Beloy, K., Kozlov, M. G., Borschevsky, A., et al. 2011, Phys. Rev. A, 83, 062514
Bergin, E. A., Phillips, T. G., Comito, C., et al. 2010, A&A, 521, L20
Botschwina, P., Seeger, S., & Flügge, J. 1993, J. Chem. Phys., 99, 8349
Cernicharo, J. 2011, EAS Publ. Ser. 58, Proc. the European Conference on Laboratory Astrophysics, 58, 251
de Almeida, A. A., & Singh, P. D. 1982, A&A, 113, 199
Dore, L., Bizzocchi, L., & Degli Esposti, C. 2012, A&A, 544, A19
Dulieu, F., Congiu, E., Noble, J., et al. 2013, Nature Sci. Rep., 3, 1338
Fazio, G. G., Lada, C. J., Kleinmann, D. E., et al. 1978, ApJ, 221, L77
Garrod, R. T., & Herbst, E. 2006, A&A, 457, 927
Garrod, R., Park, I. H., Caselli, P., & Herbst, E. 2006, Faraday Discuss., 133, 51
Garrod, R. T., Wakelam, V., & Herbst, E. 2007, A&A, 467, 1103
Garwood, R. W., & Dickey, J. M. 1989, ApJ, 338, 841
Gendriesch, R., Lewen, F., Winnewisser, G., & Müller, S. P. 2001, J. Mol. Struct., 599, 293
Godard, B., Falgarone, E., Gerin, M., et al. 2012, A&A, 540, A87
Graedel, T. E., Langer, W. D., & Frerking, M. A. 1982, ApJS, 48, 321
Harada, N., Herbst, E., & Wakelam, V. 2010, ApJ, 721, 1570
Hasegawa, T. I., Herbst, E., & Leung, C. M. 1992, ApJS, 82, 167
Hassel, G. E., Harada, N., & Herbst, E. 2011, ApJ, 743, 182
Herbst, E., & Osamura, Y. 2008, ApJ, 679, 1670
Huang, X., & Lee, T. J. 2009, J. Chem. Phys., 131, 104301
Hübers, H., Evenson, K. M., Hill, C., & Brown, J. M. 2009, J. Chem. Phys., 131, 034311
Indriolo, N., Neufeld, D. A., Gerin, M., et al. 2012, ApJ, 758, 83
Jenkins, E. B., Drake, J. F., Morton, D. C., et al. 1973, ApJ, 181, L122
Lis, D. C., & Goldsmith, P. F. 1989, ApJ, 337, 704
Monje, R. R., Emprechtinger, M., Phillips, T. G., et al. 2011, ApJ, 734, L23
Mount, B. J., Redshaw, M., & Myers, E. G. 2012, Phys. Rev. A, 85, 012519
Müller, H. S. P., & Brünken, S. 2005, J. Mol. Spectr., 232, 213
Müller, H. S. P., Thorwirth, S., Roth, D. A., & Winnewisser, G. 2001, A&A, 370, L49
Müller, H. S. P., Schlöder, F., Stutzki, J., & Winnewisser, G. 2005, J. Mol. Struct., 742, 215
Nummelin, A., Bergman, P., Hjalmarson, Å., et al. 2000, ApJS, 128, 213
Öberg, K. I., Fuchs, G. W., Awad, Z., et al. 2007, ApJ, 662, L23
Ott, J., Weiß, A., Staveley-Smith, L., Henkel, C., & Meier, D. S. 2014, ApJ, 785, 55
Otto, R., Mikosch, J., Trippel, S., Weidemüller, M., & Wester, R. 2008, Phys. Rev. Lett., 101, 063201
Persson, C. M., Black, J. H., Cernicharo, J., et al. 2010, A&A, 521, L45 (Paper I)
Persson, C. M., De Luca, M., Mookerjea, B., et al. 2012, A&A, 543, A145 (Paper II)
Pickett, H. M., Poynter, I. R. L., Cohen, E. A., et al. 1998, J. Quant. Spectr. Rad. Transfer, 60, 883
Pilbratt, G., Riedinger, J. R., Passvogel, T., et al. 2010, A&A, 518, L1
Rawat, P., Prabhudesai, V. S., Rahman, M. A., Ram, N. B., & Krishnakumar, E. 2008, Int. J. Mass Spectrom., 277, 96
Roelfsema, P. R., Helmich, F. P., Teyssier, D., et al. 2012, A&A, 537, A17
Sanna, A., Reid, M. J., Menten, K. M., et al. 2014, ApJ, 781, 108
Sharp, T. E., & Dowell, J. T. 1969, J. Chem. Phys., 50, 3024
Snow, Jr., T. P. 1976, ApJ, 204, L127
Snow, Jr., T. P. 1980, in Interstellar Molecules, ed. B. H. Andrew, IAU Symp., 87, 247
Snow, T. P., & McCall, B. J. 2006, ARA&A, 44, 367
Tack, L. M., Rosenbaum, N. H., Owrutsky, J. C., & Saykally, R. J. 1986, J. Chem. Phys., 85, 4222
van der Tak, F. F. S., Belloche, A., Schilke, P., et al. 2006, A&A, 454, L99
van der Tak, F. F. S., Black, J. H., Schöier, F. L., Jansen, D. J., & van Dishoeck, E. F. 2007, A&A, 468, 627
Verhoeve, P., Ter Meulen, J. J., Meerts, W. L., & Dyamanus, A. 1986, Chem. Phys. Lett., 132, 213
Wakelam, V., & Herbst, E. 2008, ApJ, 680, 371
Wickham-Jones, C. T., Ervin, K. M., Ellison, G. B., & Lineberger, W. C. 1989, J. Chem. Phys., 91, 2762
Wirström, E. S., Bergman, P., Black, J. H., et al. 2010, A&A, 522, A19
Xu, L.-H., Fisher, J., Lees, R. M., et al. 2008, J. Mol. Spectr., 251, 305

Appendix A: Modelling the CH$_2$NH absorption lines

CH$_2$NH has two transitions with similar line strengths close to NH$^+$ at 1013 GHz: $3_{3,1}-2_{2,0}$ (1012.531 GHz) with $E_1 = 41$ K only +8.5 MHz (-2.5 km s^{-1}) from NH$^+$, and $3_{3,0}-2_{2,1}$ (1012.661 GHz) seen as a narrow absorption at 21 km s^{-1}. It should be noted that this line blends with the SO$_2$ $41_{5,37}-40_{4,36}$ (1012.673 GHz) emission. We model the SO$_2$ emission, both CH$_2$NH absorptions, and the o-NH$_2$ $4_{2,2}-4_{1,3}$ emission line wing (seen at $\sim$70 km s^{-1}) in order to subtract these lines in the search for any remaining weak NH$^+$ absorption. All modelled lines are shown in Fig. A.2 together with the original data in black and the resulting spectra after subtraction of the above described lines is shown in red.
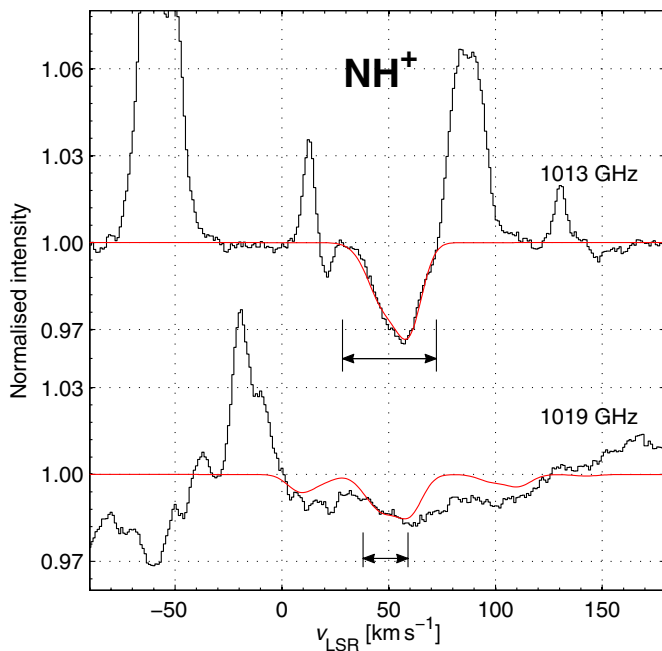
Fig. A.1. Sgr B2 (M). Gaussian fits of NH$^+$ 1013 and 1019 GHz line profiles, including all hfs components, to the observations. The arrows mark the velocity range in which the fit was made.
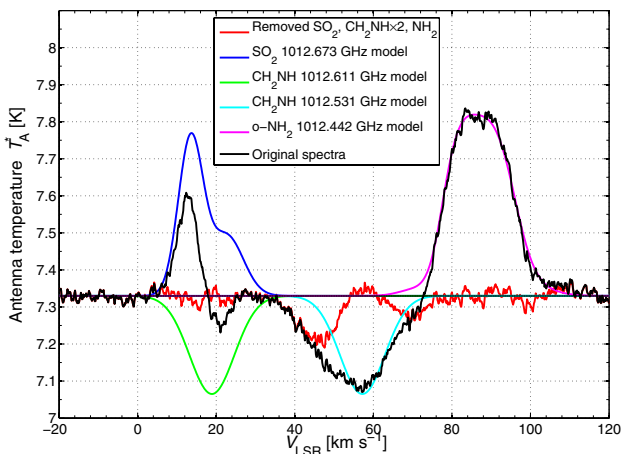
Fig. A.2. Sgr B2 (M). Observed NH$^+$ 1013 GHz search spectrum (black) along with models of the two absorbing CH$_2$NH transitions (green and cyan), the expected SO$_2$ (blue) and NH$_2$ (pink) emissions, and the remaining spectrum after removal of their expected contributions (red; more details in Sect. 3).
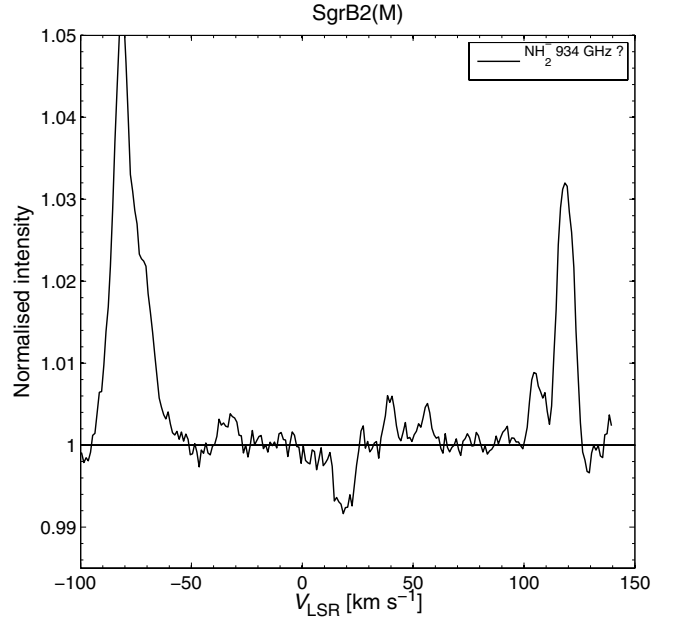
Fig. A.3. Absorption feature found at a velocity of +18.5 km s^{-1} is tentatively identified as p-NH$_2^-$ from the source molecular cloud. We use the resulting integrated opacity as an upper limit to N(NH$_2^-$). The emission line at 110 km s^{-1} is methanol $9_{2,7}-8_{1,8}$ (rest frequency 933.693 GHz).

The numerous SO$_2$ lines observed in our band (e.g. $39_{5,35}-38_{4,34}$ and $43_{5,39}-42_{4,38}$), as well as in the HEXOS spectral line survey, are used to reconstruct the SO$_2$ 1012.673 GHz line. The true CH$_2$NH absorption is then found by comparing the reconstructed SO$_2$ emission with the observed line profile. Finally, the modelled CH$_2$NH absorption is used as a template for the CH$_2$NH absorption at 1012.531 GHz since their line strengths are similar. We use RADEX to check our modelled CH$_2$NH lines together with the 225 GHz ($1_{1,1}-0_{0,0}$) line observed in absorption by Nummelin et al. (2000). The integrated opacities of these three lines are matched using a density of n(H$_2$) $\sim 10^5$ cm^{-3}, a kinetic temperature of $\sim$100 K, a column density N(CH$_2$NH) $\sim 1 \times 10^{15}$ cm^{-2}, and a line width of $\sim$15 km s^{-1} which supports the above modelling and results. After subtracting all modelled lines, we find a weak remaining absorption feature at $V_{LSR} = 69$ km s^{-1} with an integrated opacity of 0.08 km s^{-1}, which is used as an upper limit to NH$^+$.

Appendix B: NH$_2^-$ chemistry

The NH$_2^-$ anion can form via the dissociative attachment process through electron-impact on NH$_3$

$$e^* + NH_3 \rightarrow NH_2^- + H, \tag{B.1}$$

where e^* represents an energetic electron. The energetic threshold for this process is $\varepsilon = 3.857$ eV, potentially leading to an unusually high production rate. At kinetic temperatures of the order of 100 K or less, the thermal electrons have a characteristic energy less than 9 meV. Therefore, the hot electrons required to form the anion are extremely superthermal. A self-consistent treatment of the electron speed distribution in the weakly ionised interstellar medium is currently being investigated (Black, in prep.). The crucial energy range for reaction (B.3) is 3.8 to 8.5 eV. In photon-dominated regions, including diffuse molecular clouds, such electrons are produced mainly by the same photoelectric effect involving dust and large

molecules that dominates the heating of the gas. Energetic electrons are thermalised primarily by collisions with neutrals (H and H$_2$), rather than by elastic collisions with thermal electrons, as long as the fractional ionisation is less than 10^{-3}. The cross-section, σ_{DA}, for the dissociative attachment process has a peak value of 1.6 Mb near $\varepsilon = 5.8$ eV, with vanishing values at $\varepsilon < 4.2$ and at $\varepsilon > 8.5$ eV (Sharp & Dowell 1969; Rawat et al. 2008). The number density of electrons integrated over the interval 3.857 to 8.5 eV is 9.9×10^{-8} cm^{-3}. We find a production rate for NH$_2^-$ by reaction (B.3) of

$$\int n_e(\varepsilon)\,\sigma_{DA}(\varepsilon)\,\upsilon\,d\varepsilon = 7.0 \times 10^{-18} \;\; [\text{s}^{-1} \text{ per NH}_3]. \tag{B.2}$$

The possible destruction processes of NH$_2^-$ include photo-detachment, reactions with H$_2$, and mutual neutralisation in reactions with the most abundant positive ions. The reaction with H$_2$,

$$\text{NH}_2^- + \text{H}_2 \rightarrow \text{NH}_3 + \text{H}^-, \tag{B.3}$$

is known to be rapid at low temperatures around 20 K but to decrease with increasing temperature (Otto et al. 2008). If the reaction with H$_2$ is the dominant loss process, then the density of NH$_2^-$ at $T = 50-100$ K will be of the order of

$$n(\text{NH}_2^-) \sim 7 \times 10^{-8}\, \frac{n(\text{NH}_3)}{n(\text{H}_2)} \;\; [\text{cm}^{-3}], \tag{B.4}$$

which immediately suggests a very low NH$_2^-$ abundance.

A second formation route of NH$_2^-$ is via slow radiative attachment of electrons to NH$_2$

$$\text{NH}_2 + \text{e}^- \longrightarrow \text{NH}_2^- + h\nu. \tag{B.5}$$
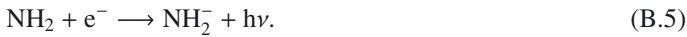
Radiative attachment via emission from excited vibrational states has been calculated to be an efficient process to produce negative molecular ions with large electron affinities (3−4 eV) and at least four atoms (Herbst & Osamura 2008). The NH$_2^-$ anion is smaller than this limit and has only a moderate electron affinity of 0.771 eV (Wickham-Jones et al. 1989). Using Eq. (11)

in Herbst & Osamura (2008), we estimate the rate coefficient for radiative attachment via the vibrational mechanism to be only $1 \times 10^{-17}(T/300$ K$)^{-1/2}$ cm^3 s^{-1}. The process is at most competitive with dissociative attachment of NH$_3$ via non-thermal electrons, and does not change the conclusion that the NH$_2^-$ anion has a low abundance. Finally, if the anion is formed in a local region rich in atomic rather than molecular hydrogen, it can be destroyed by associative attachment with atomic hydrogen,

$$\text{NH}_2^- + \text{H} \longrightarrow \text{NH}_3 + \text{e}^-, \tag{B.6}$$

or competitively via photo-detachment.

Appendix C: Chemical models
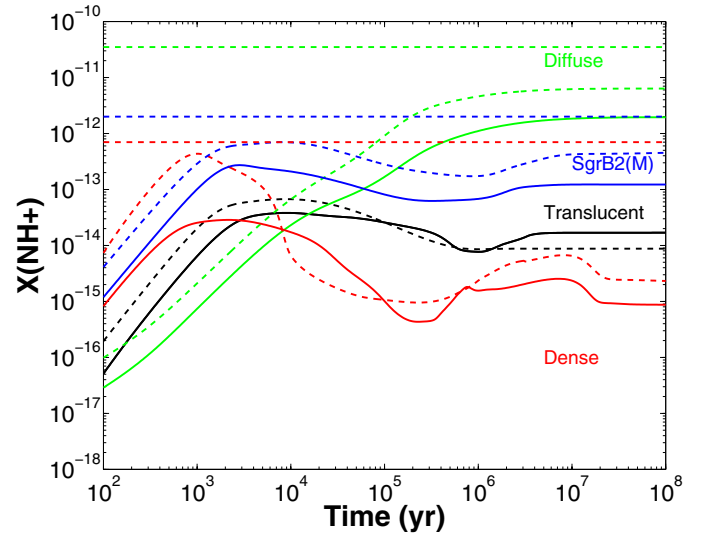
Fig. C.1. Temporal evolution of the NH$^+$ abundance for all four models (Table 3) where each model is plotted with a high metal abundance (dashed lines) and with a low metal abundance (solid lines). The translucent and dense models are plotted for $T_K = 30$ K alone. The observed upper limits are indicated with dashed horizontal lines following the respective model colour code.
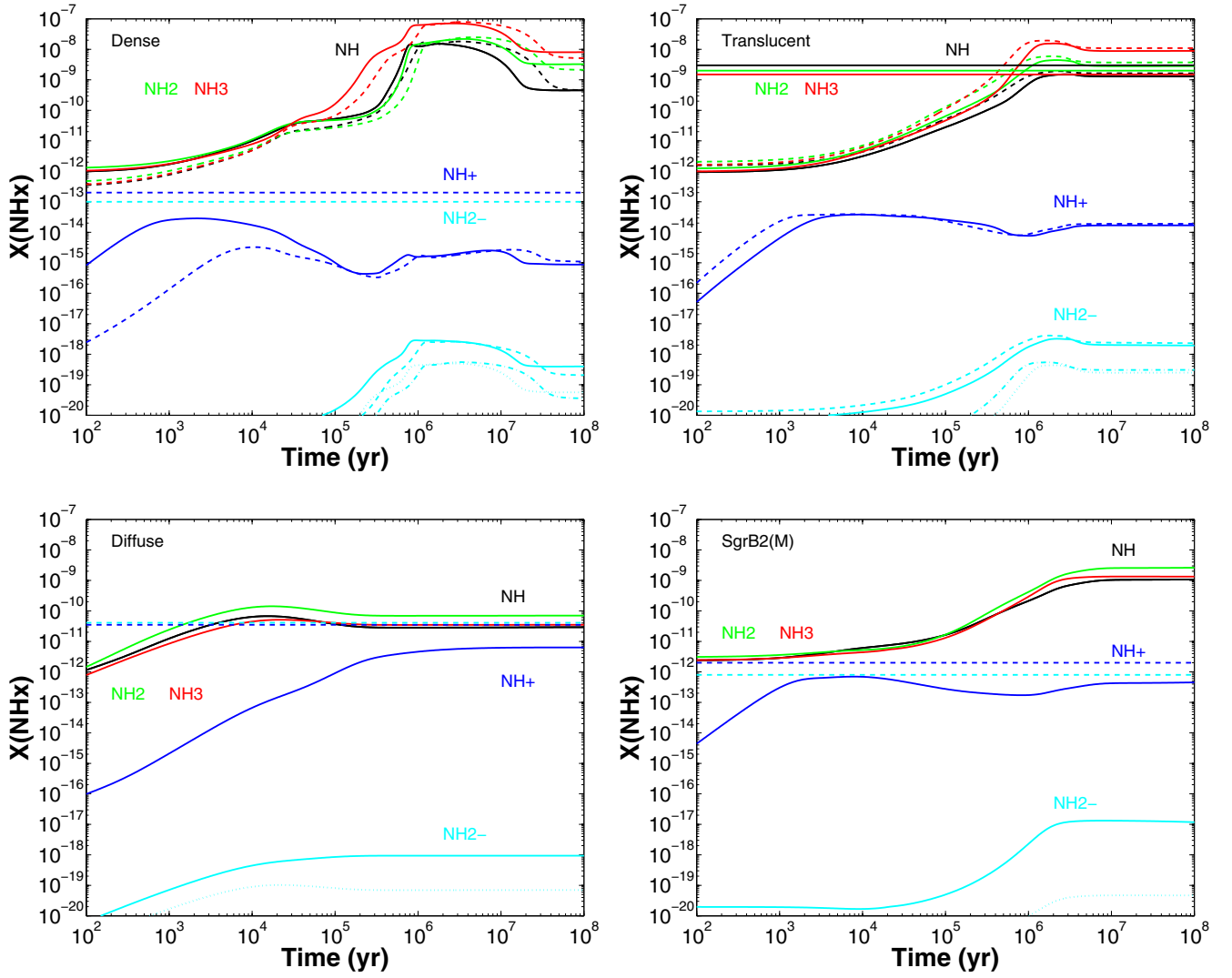
Fig. C.2. Temporal evolution of the nitrogen hydride abundances. *Upper left*: dense gas; *upper right*: translucent gas; *lower left*: diffuse gas; *lower right*: Sgr B2 (M) envelope model (see Table 3). The dot-dashed and dotted lines for NH$_2^-$ represent the estimated $X(\mathrm{NH}_2^-) \sim 7 \times 10^{-8} \times X(\mathrm{NH}_3)$ for the T_K = 30 K and 50 K (translucent) and T_K = 30 K and 10 K (dense) models. The observed abundances and upper limits corresponding to the different models are indicated with solid and dashed horizontal lines, respectively, following the respective species colour code.
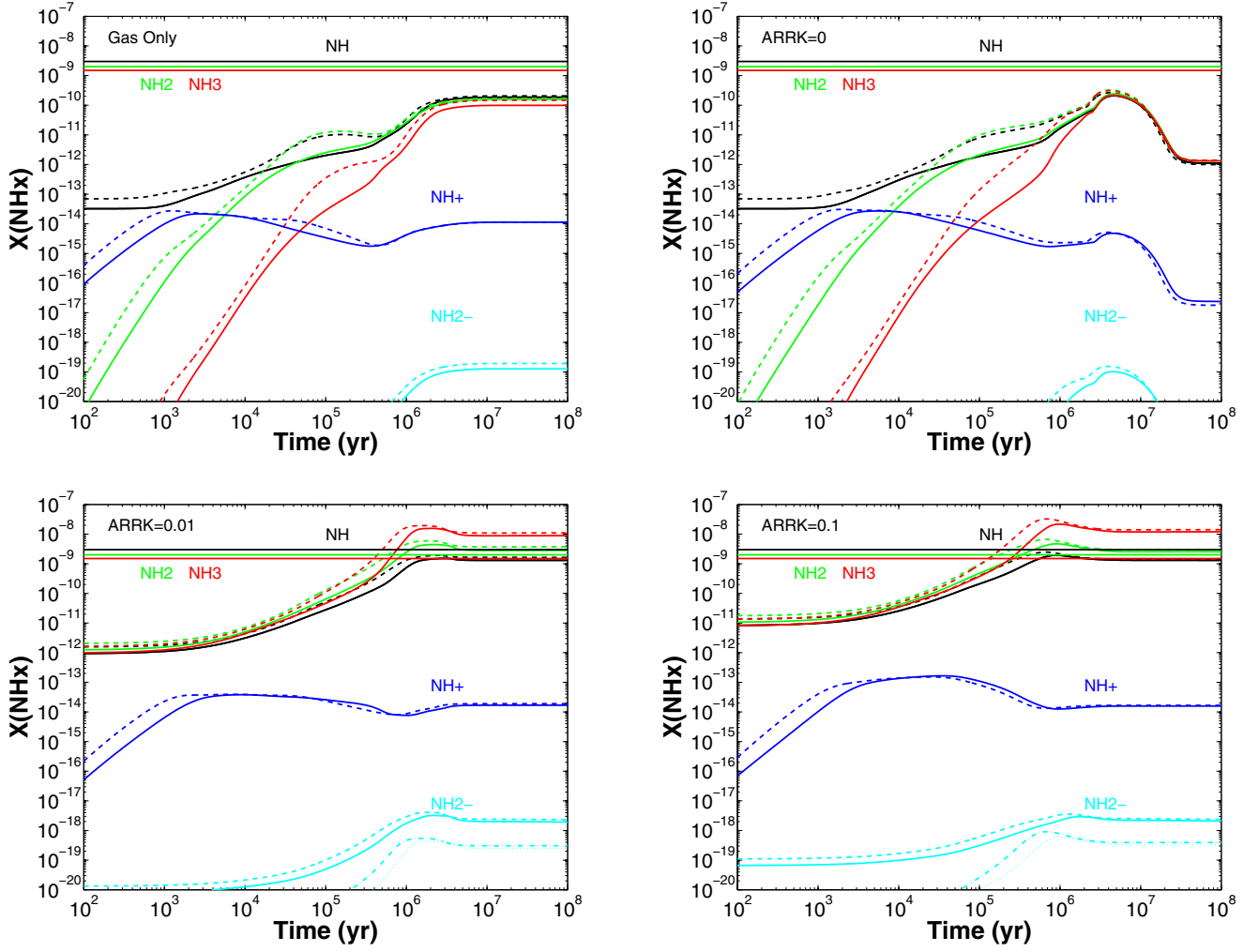
Fig. C.3. Translucent gas conditions in all models (see Table 3). *Upper left*: pure gas phase chemistry. *Upper right*: gas and surface chemistry and inactive non-thermal desorption efficiency $a_{RRK} = 0$. *Lower left*: gas and surface chemistry and active non-thermal desorption with the typical efficiency $a_{RRK} = 0.01$. *Lower right*: gas and surface chemistry and high active non-thermal desorption ($a_{RRK} = 0.1$). The observed abundances and upper limits are indicated with solid and dashed horizontal lines, respectively, following the respective species colour code. The dot-dashed and dotted lines for NH$_2^-$ represent the estimated $X(\mathrm{NH}_2^-) \sim 7 \times 10^{-8} \times X(\mathrm{NH}_3)$ for the $T_K = 30$ K and 50 K models. If the reactive desorption mechanism is active with the typical $a_{RRK} = 0.01$, each NH, NH$_2$ and NH$_3$ species that is formed on the grain through a hydrogenation reaction has a probability of 9.3×10^{-3}, 7.6×10^{-3}, and 5.2×10^{-3}, respectively, to desorb into the gas phase. There it will become available for detection and for follow-up reactions. Experiments by Dulieu et al. (2013) indicate that this type of non-thermal desorption could be much more efficient on bare grains than $a_{RRK} = 0.01$. As shown, our models are not very sensitive to the exact value of the desorption probability, since the model with $a_{RRK} = 0.1$ gives very similar results to the model using $a_{RRK} = 0.01$.
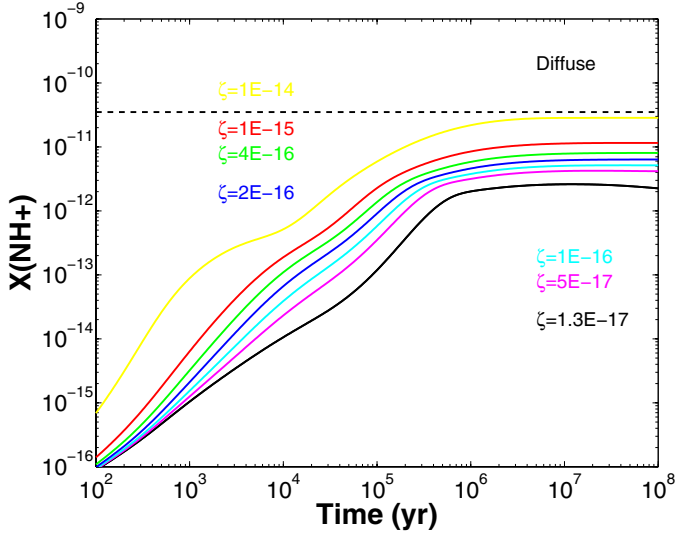
Fig. C.4. Temporal evolution of the NH$^+$ abundance for different cosmic ray ionisation rates for diffuse gas conditions (Table 3). The dashed black line represents the observed upper NH$^+$ limit in the diffuse gas.

Appendix D: Tables

Table D.1. Hyperfine structure components of NH$^+$ $^2\Pi_{1/2}$ $N = 1-1$, $J = 1.5^- - 0.5^+$.

Frequency (GHz)	A_{ul} (s^{-1})	g_u	Δv^a (km s^{-1})	Rel. Intensity^b $\frac{A_{ul} \times g_u}{A_{ul}(main) \times g_u(main)}$
1012.516	0.00885	5	1.9	0.47
1012.523	0.01358	7	0	1
1012.529	0.00903	3	−1.8	0.28
1012.533	0.00193	3	−3.0	0.06
1012.534	0.00208	5	−3.4	0.11
1012.550	0.00265	5	−8.1	0.14
1012.556	0.00471	5	−10	0.25
1012.556	0.00703	3	−10	0.22
1012.567	0.00261	3	−13	0.08
1012.570	0.00887	1	−14	0.09
1012.571	0.00857	5	−14	0.45
1012.574	0.00226	3	−15	0.07
1012.589	0.00427	3	−20	0.13
1012.604	0.00471	1	−24	0.05

Notes. $^{(a)}$ The velocity offset from the strongest hfs component at 1012.523 GHz. $^{(b)}$ The sum of the relative intensities of the 14 hfs components is 3.4.

Table D.2. Hyperfine structure components of NH$^+$ $^2\Pi_{1/2}$ $N = 1-1$, $J = 1.5^+ - 0.5^-$.

Frequency (GHz)	A_{ul} (s^{-1})	g_u	Δv^a (km s^{-1})	Rel. Intensity^b $\frac{A_{ul} \times g_u}{A_{ul}(main) \times g_u(main)}$
1018.911	0.00137	3	83	0.04
1019.013	0.00095	3	53	0.03
1019.020	0.00566	5	51	0.29
1019.060	0.00434	3	39	0.13
1019.067	0.00113	5	37	0.06
1019.184	0.00130	5	2.5	0.07
1019.193	0.01392	7	0	1.00
1019.229	0.00381	3	−11	0.12
1019.232	0.01247	5	−11	0.64
1019.251	0.01328	1	−17	0.14
1019.259	0.00813	3	−20	0.25
1019.330	0.00547	3	−40	0.17
1019.361	0.00315	3	−49	0.10
1019.368	0.00713	5	−51	0.37

Notes. $^{(a)}$ The velocity offset from the strongest hfs component at 1019.193 GHz. $^{(b)}$ The sum of the relative intensities of the 14 hfs components is 3.4.

Table D.3. Para-NH$_2^-$ $^1A_1$, $J_{K_a,K_c} = 1_{1,1} - 0_{0,0}$. Spectroscopic data from Tack et al. (1986). See Sect. 2 for more details.

Frequency^a (GHz)	Error^b (MHz)	$A_{ul}{}^c$ (s^{-1})	E_u (K)
933.855	≳100	5.43e-03	45

Notes. $^{(a)}$ Cernicharo (2011). $^{(b)}$ Error of predicted frequency. $^{(b)}$ Using a ground state dipole moment of 1.311 Debye (estimated uncertainty is 0.01 D; Botschwina et al. 1993).

Table D.4. *Herschel* OBSID's of the observed transitions analysed in this paper.

Source	Species	Frequency (GHz)	Band	LO-setting[a]	Date	OBSID
G10.6-0.4	NH^+	1 012.540	4a	A	2012-04-10	1342244052
				B		1342244053
				C		1342244054
		1 019.210	4a	A	2012-04-10	1342244055
				B		1342244056
				C		1342244057
	p-NH_2^-	933.855	3b	A	2012-09-18	1342251113
				B		1342251114
				C		1342251115
Sgr B2 (M)	NH^+	1 012.540	4a	SScan	2012-04-04	1342243701
		1 019.210	4a	SScan	2012-04-04	1342243702
	p-NH_2^-	933.855	3b	SScan	2012-09-18	1342251112

Notes. [a] Three different frequency settings of the LO were performed towards G10.6−0.4, with approximately 15 km s^{-1} between each setting in order to determine the sideband origin of the signals. Towards Sgr B2 (M) we used the spectral scan mode with 8 different LO settings.

Table D.5. Initial elemental abundances.

Species i	n_i/n_H high metal[a,b]	n_i/n_H low metal[a,c]
H	1	. . .
H_2	. . .	0.5
He	0.09	0.14
C^+	1.4(–4)	7.3(–5)
N	7.5(–5)	2.14(–5)
O	3.2(–4)	1.76(–4)
S^+	1.5(–6)	8.0(–8)
Na^+	2.0(–8)	2.0(–9)
Mg^+	2.55(–6)	7.0(–9)
Si^+	1.95(–6)	8.0(–9)
P^+	2.3(–8)	3.0(–9)
Cl^+	1.4(–8)	4.0(–9)
Fe^+	7.4(–7)	3.0(–9)

Notes. [a] $x(y) = x \times 10^y$. [b] Adopted from Garrod & Herbst (2006) and Wakelam & Herbst (2008). [c] Adopted from Garrod et al. (2007), based on Graedel et al. (1982).